Supplementary Information

Ultrasmall Co$_3$O$_4$ nanoparticles as long-lived high-rate lithium-ion battery anode

*Ping Wan, [a] Yang Si, [a] Shuang Zhu, [a] Changda Wang, [a] Yuyang Cao, [a] Zhen Yu, [b] Wenjie Wang, [a] Chen Chen, [a] Wangsheng Chu, *[a] and Li Song, [a]*

a. National Synchrotron Radiation Laboratory, University of Science and Technology of China, Hefei, Anhui 230029, P. R. China
b. Hefei Institute for Advanced Research, Anhui University of Science and Technology, Hefei, Anhui 231131, P.R. China.

E-mail: chuws@ustc.edu.cn

Keywords: cobalt oxide, ultrasmall nanoparticles, particle size effect, lithium ion batteries

1. Experimental

1.1 Synthesis of the precursor Co-PBA nanoparticles

In a typical procedure, 3 mmol K$_3$Co(CN)$_6$, 5.6 g PVP (K40) and 6 mmol CoCl$_2$·6H$_2$O were dissolved into a mixed solution of 25 mL ethanol and 75 mL deionized water. The obtained pink solution was kept away from light for 24 h after stirred for 2 h. Then it was centrifuged and washed for several times with deionized water and ethanol and finally dried overnight at 100 °C under vacuum.

1.2 Synthesis of the ultrasmall S-Co$_3$O$_4$ nanoparticles

The collected precursor Co-PBAs were crystallized at 360 °C for 1 h at a heating rate of 1 °C min^{-1} under an air atmoparticle.

By the way, the comparison sample C-Co_3O_4 (commercial Co_3O_4) was just purchased from the Internet (Sinopharm Chemical Reagent Co., Ltd., SP).

1.3 Materials characterization

The XRD patterns were recorded on a D8-Advance power diffractometer equipped with a Cu Kα radiation source ($\lambda = 1.54178$ Å). The morphology of these samples was characterized by a field emission scanning electron microscopy (15 kV, JEOL, JSM-6700F) and TEM (JEOL JEM2010). Thermogravimetry (TG) measurement was carried out on a NETZSCH TG 209F1 Libra instrument in air flux at a scan rate of 10 °C min^{-1}. Brunauer–Emmett–Teller (BET) surface areas were measured using Tristar II 3020 instrument by nitrogen adsorption at 77 K. Raman spectra were obtained from a LabRamHR using an argon ion laser with a wavelength of 785 nm. Co K-edge X-ray absorption fine structure (XAFS) was recorded at the 1W2B beamline of the Beijing Synchrotron Radiation Facility (BSRF, Beijing). X-ray absorption near edge structure (XANES) and extended X-ray absorption fine structure (EXAFS) data were both analysed by the ATHENA software package. To further obtain the magnitudes of the EXAFS spectra in R-space (Å), the extracted EXAFS signal was Fourier-transformed in k-ranges of 2.4-12.5 Å^{-1} by using a Hanning window function after weighted by k^2. The lengths of actual bond are approximately 0.2-0.4 Å longer because the Fourier-transformed peaks were not phase corrected. The soft X-ray absorption spectroscopy

(s-XAS) of Co L-edge was collected at the BL12B-a (MCD) line station of the Hefei Synchrotron Radiation Facility (HALF). To get the desired electrodes, the coin cells, which were charged or discharged to the desired cut-off voltages, have been disassembled by an electric crimping machine (MTI Co.). Finally, electrodes were washed with dimethyl carbonate (DMC) and sealed by a 3 M sellotape in Ar atmoparticle after drying. The electrodes for XAFS and s-XAS were collected after fully charged or discharged for three or four cycles.

1.4 Electrochemical measurements

The battery tests were carried out in a half-cell configuration. Lithium disc was used as a counter electrode to assemble the CR2032-type coin cells, and all the processes were carried out in a glovebox filled with argon (MBraun, Germany). The working electrode consists of active materials, conductivity agent (Ketjenblack), and polymer binder (polyvinylidene fluoride, PVDF) with a weight ratio of 7:2:1. After mixed fully in N-methyl-2-pyrrolidinone, the obtained slurry was casted on Cu foil and dried at 110°C under vacuum overnight. After drying, slice to obtain circular electrodes with a diameter of 16 mm. The mass loading of the active material was 0.5-1 mg cm^{-2}. The electrolyte was a solution of 1 M LiPF$_6$ in ethylene carbonate/dimethyl carbonate (EC/DMC, 1:1 in weight). Whatman Glass Microfibre Filter (Grade GF/D) were used as separator. The electrochemical performance of the cells was assessed on a Land CT2001A cell test system (Wuhan, China) in the range of 0.01-3 V (vs. Li$^+$/Li). Cyclic voltammetry (CV) was measured from 0.01 to 3 V (vs. Li$^+$/Li) at the scan rate of 0.2

mV s^{-1}. Electrochemical impedance spectroscopy (EIS) testing with an amplitude of 10

mV from 10^5 Hz to 0.01 Hz. EIS and CV were both obtained on a CHI660D (Chenhua,

Shanghai) electrochemical workstation.
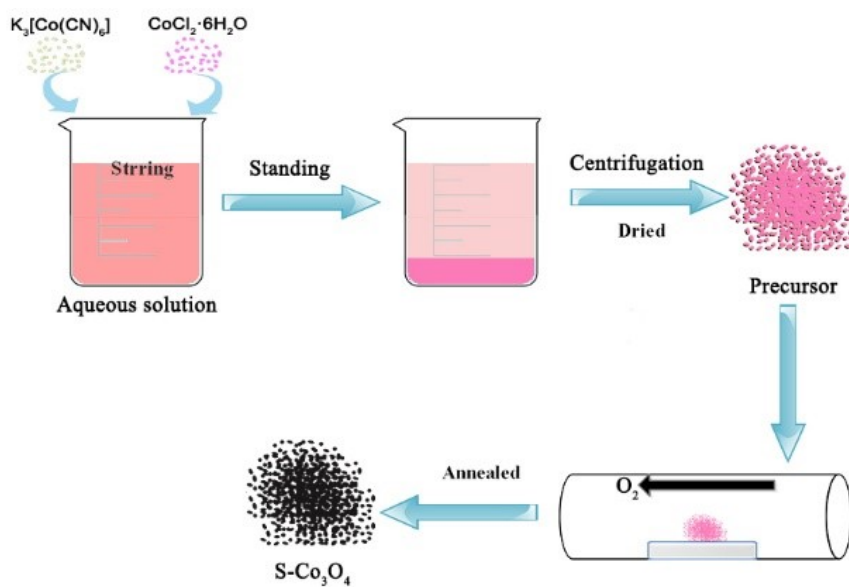
2. Rusults and discussion

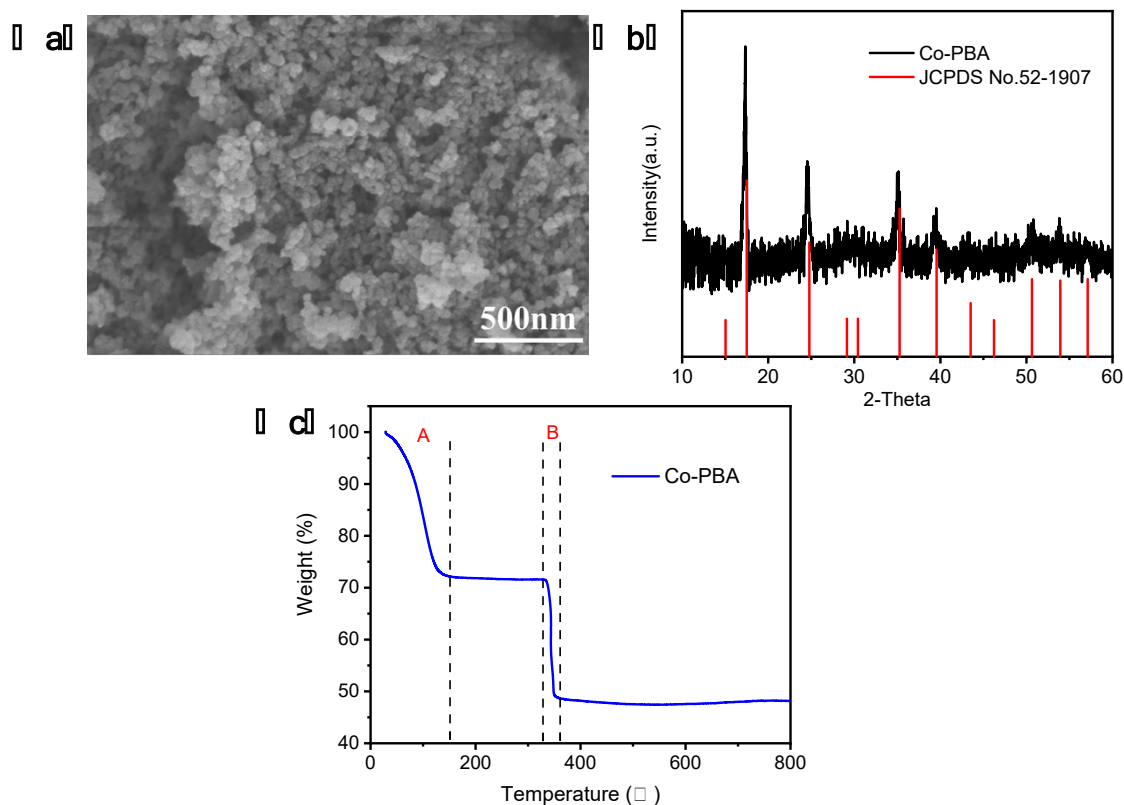**Figure S1.** Diagrammatic sketch of synthesis process for S-Co$_3$O$_4$ spinel sample.

Figure S2. (a) SEM image, (b) XRD pattern and (c) TG curves of the precursor Co-PBA nanoparticles.

As shown in Fig. S2b, Co-based Prussian blue analogues (Co-PBA) can be indexed as a typical face-centered cubic structure (JCPDS no. 52-1907) with no impurity phase. Thermogravimetric (TG) characteristic (Fig. S2c) was employed to determine the optimum calcination temperature of the precursor. With temperature rising, the first mass drop occurs below 160 ℃, corresponding to the loss of the adsorbed and interstitial water. The second drop occurs at 330-355 ℃, corresponding to the phase transition to oxide. At subsequent temperatures up to 800 ℃, the substance stabilizes

as Co_3O_4. Take hint from the TG data, phase-pure Co_3O_4 was successfully prepared by annealing the precursor at 360 ℃.
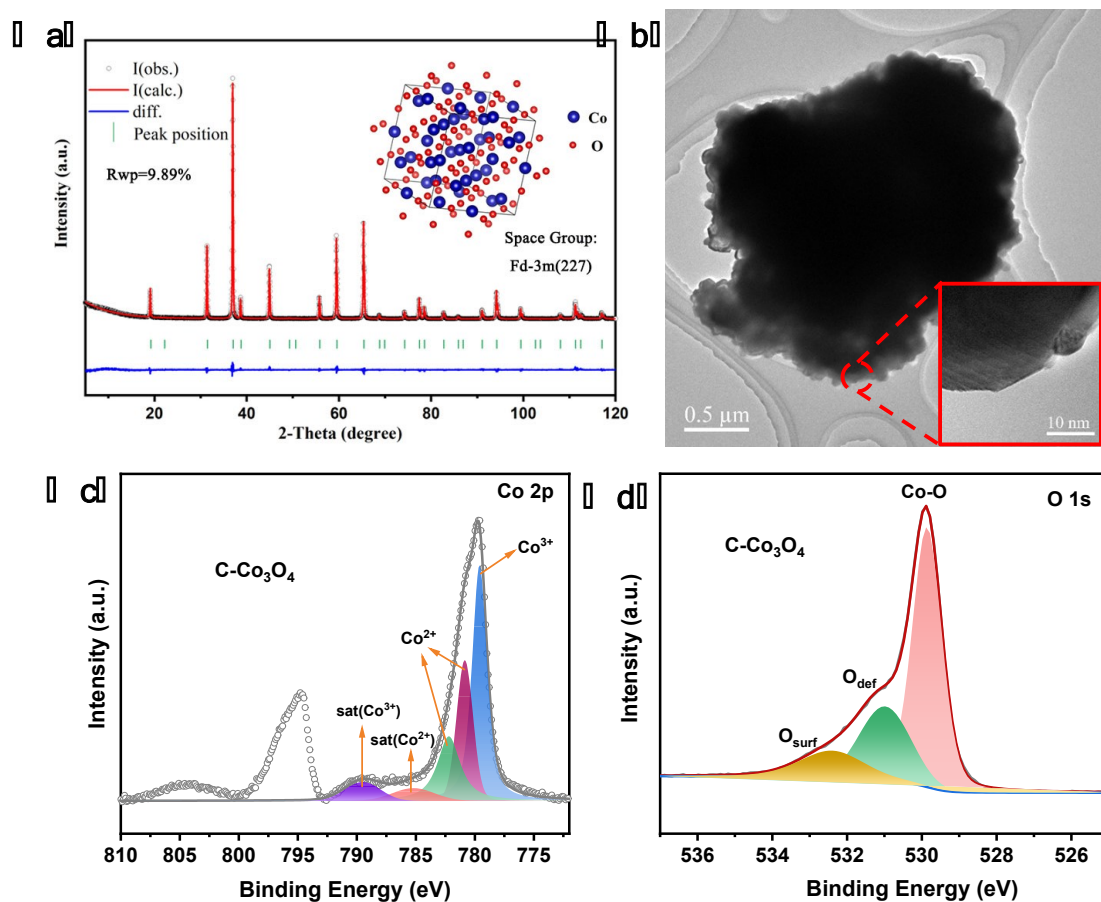

Figure S3. Structural and morphology characterization of the C-Co3O4. (a) Rietveld refinement of the PXRD data (a=b=c=8.066 Å); (b) TEM image and a magnified view; XPS analysis of (c) Co 2p and (b) O 1s.
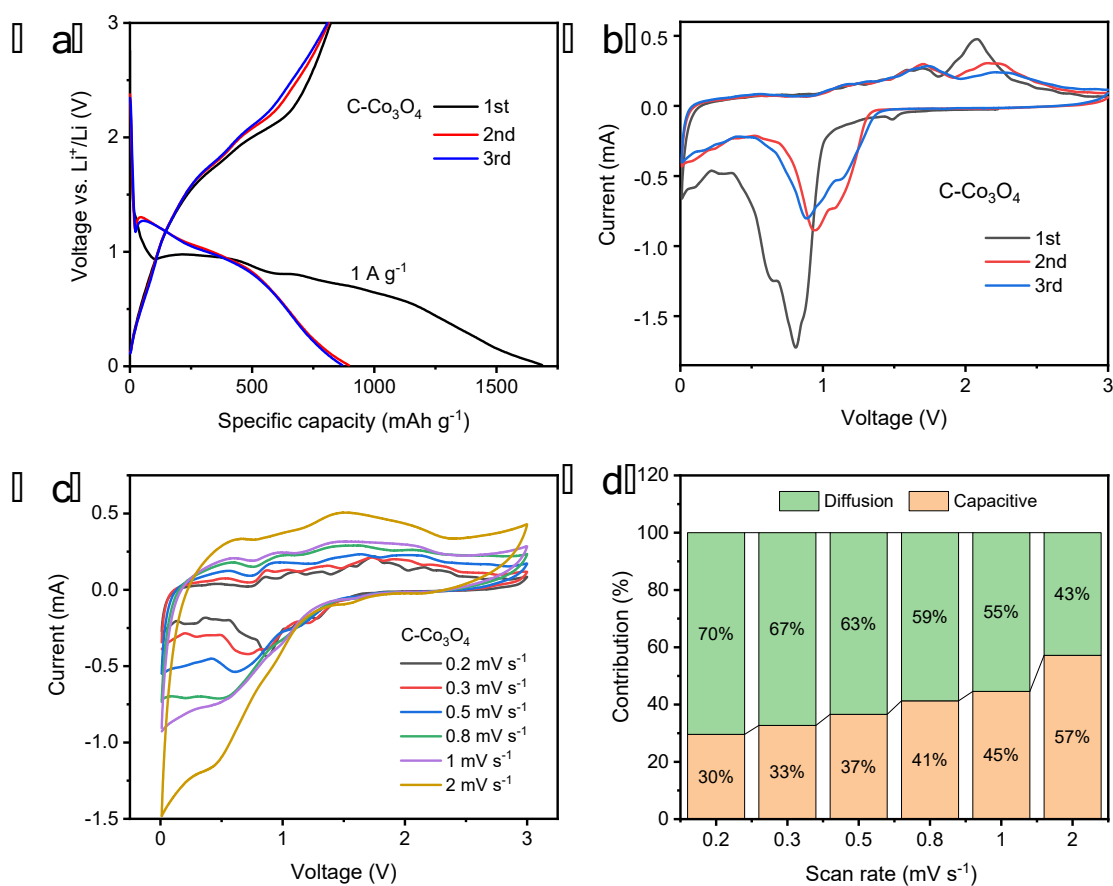
Figure S4. Electrochemical performance and kinetic analysis of C-Co$_3$O$_4$ forlithium storage behavior. (a) Charge/discharge curves at 1 A g^{-1}; (b) CV data at 0.2 mV s^{-1}; (c) CV curves obtained with various scan rates; (d) The calculated contribution ratio of the capacitive and diffusion-controlled capacities at different scan rates.

The electrochemical reactions are summarized as follow:

Discharge: $Co_3O_4 + 8Li^+ + 8e^- \rightarrow 4Li_2O + 3Co$

Charge: $4Li_2O + 3Co \rightarrow Co_3O_4 + 8Li^+ + 8e^-$
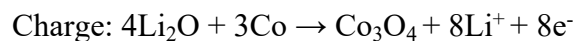
The theoretical capacity of Co$_3$O$_4$ is 890 mAh g^{-1}. The calculation is the following: C=nF/3.6M, where C is the theoretical specific capacity, n is the electron transfer

number (n=8), F is the Faraday constant ($F = 96485\ \text{C mol}^{-1}$), and M is the relative molecular mass ($M=240.8\ \text{g mol}^{-1}$).
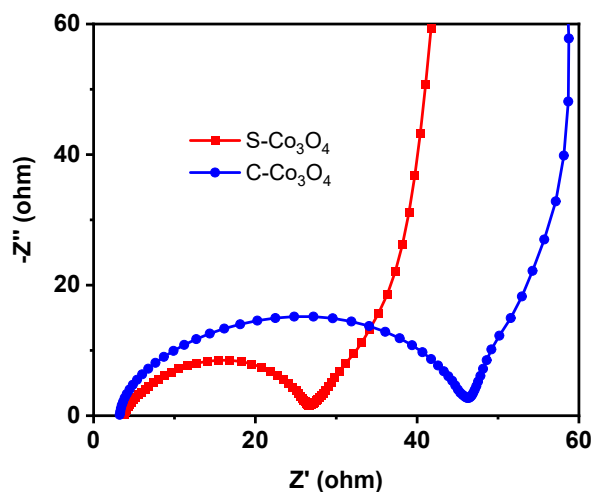

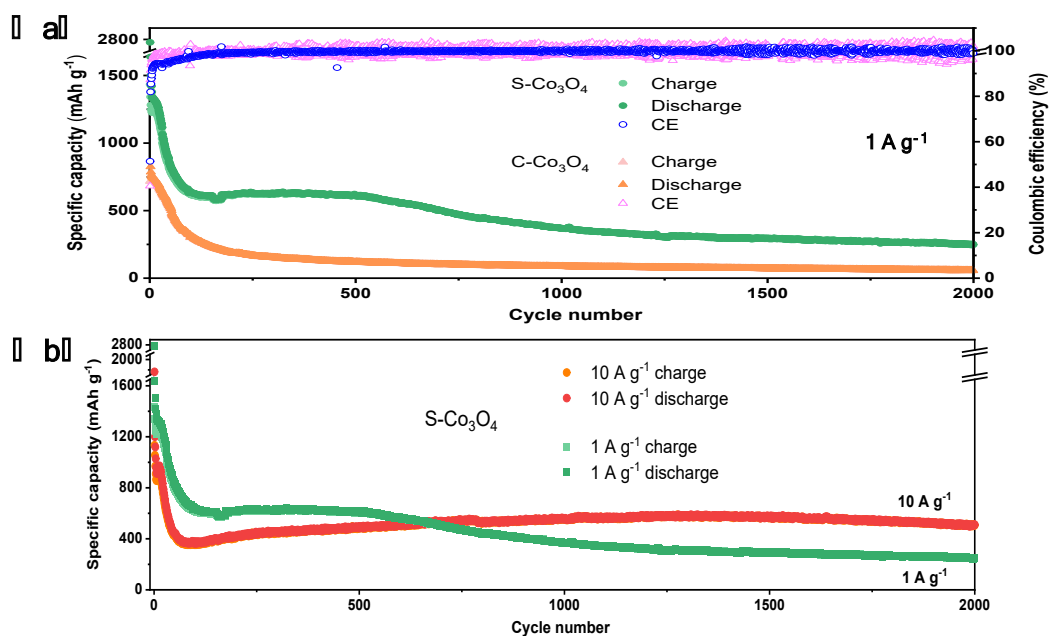**Figure S5.** The impedance spectra of S-Co$_3$O$_4$ anode and C-Co$_3$O$_4$ anode .

Figure S6. (a) Cycling performance at 1 A g^{-1} of both S-Co_3O_4 and C-Co_3O_4; (b)

Cycling performance of S-Co_3O_4 at 10 A g^{-1} and 1 A g^{-1}.

As for the performance at 1 A g^{-1} in Fig. S6a, for S-Co_3O_4 electrode, a splendid

electrochemical performance could also be found until the 510th cycle with over 610

mAh g^{-1} capacity. Then the capacity started to decline, and finally exhibited 249.7 mAh

g^{-1} at the 2000th cycle. The capacity of C-Co_3O_4 is evidently worse than that of S-Co_3O_4,

which is also because that the large micro size brought less active sites and more serious

structure collapse. Additionally, the steady capacity for S-Co_3O_4 electrode at 10 A g^{-1}

at the 2000th cycle (511.2 mAh g^{-1}) is amazingly superior than that at 1 A g^{-1} at the same

cycle (249.7 mAh g^{-1}, Fig. S6b), which may be the result of different distribution of

components in SEI at different current densities (Fig. S10), verify the superiority of the
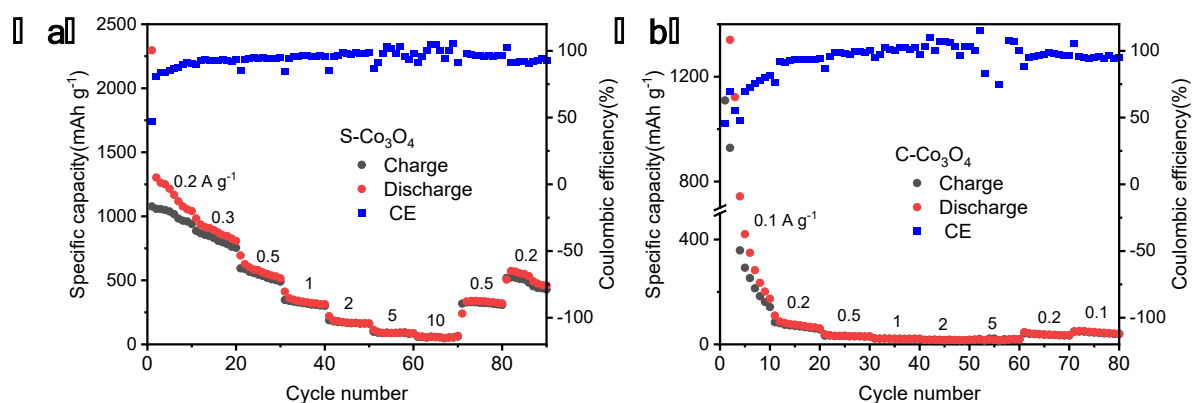
long-cycle high-rate application of S-Co_3O_4.

Figure S7. Rate performance of (a) S-Co_3O_4 and (b) C-Co_3O_4.

The rate performance of the S-Co_3O_4 electrode is measured at 0.2, 0.3, 0.5, 1, 2, 5, 10, 0.5 and 0.2 A g^{-1} every ten cycles (Fig. S7a†), and the reversible capacities are 1303.0, 936.4, 626.6, 360.1, 186.9, 98.7, 61.1, 334.7 and 572.4 mAh g^{-1}, respectively. As for the C-Co_3O_4 electrode, it presents a reversible capacity of 1121.9, 87.5, 35.1, 22.2, 16.1, 18.1, 42.3 and 51.1 mAh g^{-1} at the current of 0.1, 0.2, 0.5, 1, 2, 5, 0.2 and 0.1 A g^{-1}, respectively.
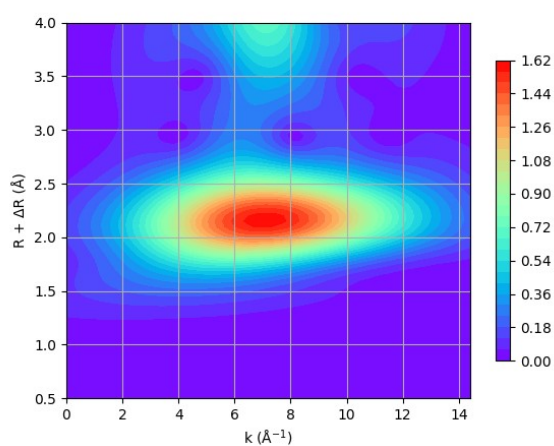

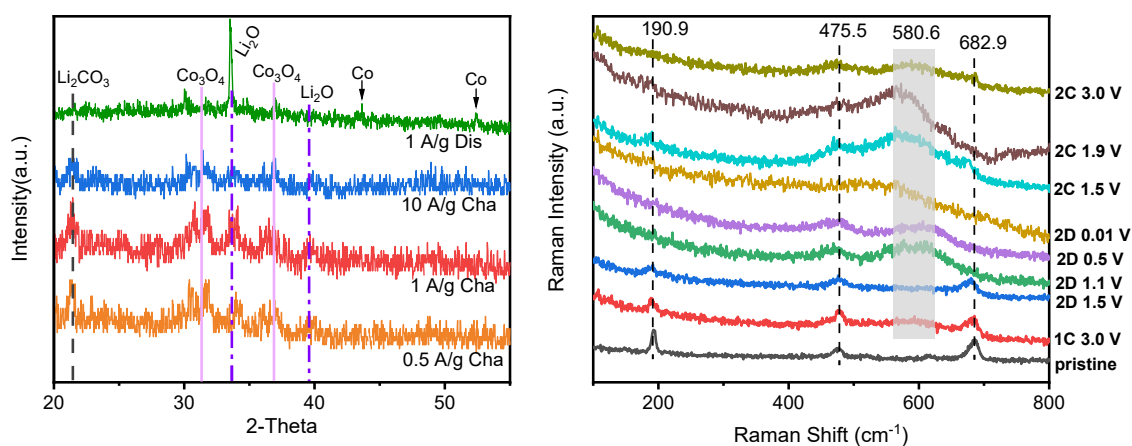**Figure S8.** WT contour plots of Co-foil.

Figure S9. (a) Ex situ XRD patterns of S-Co_3O_4 electrodes collected after fully discharged and fully charged after 10 cycles at different current densities; (b) Ex situ Raman spectra of S-Co_3O_4 electrodes collected during the first and the second diacharge/charge process.

For ex situ XRD, the fully charged electrodes at different current density are mainly Co_3O_4 accompanied by little residual Li_2O and Li_2CO_3 in SEI layer, while the fully discharged electrode is mainly Co metal and Li_2O. For ex situ Raman, 1C, 2D and 2C denote the first charge, the second discharge and the second charge, respectively. The peaks located at 190.9, 475.8 and 682.9 cm^{-1} are related to Co_3O_4, and the appearance of the broad peak at around 580.6 cm^{-1} is due to Li_2O and the homogeneous phase $Li_xCo_3O_4$.[1]
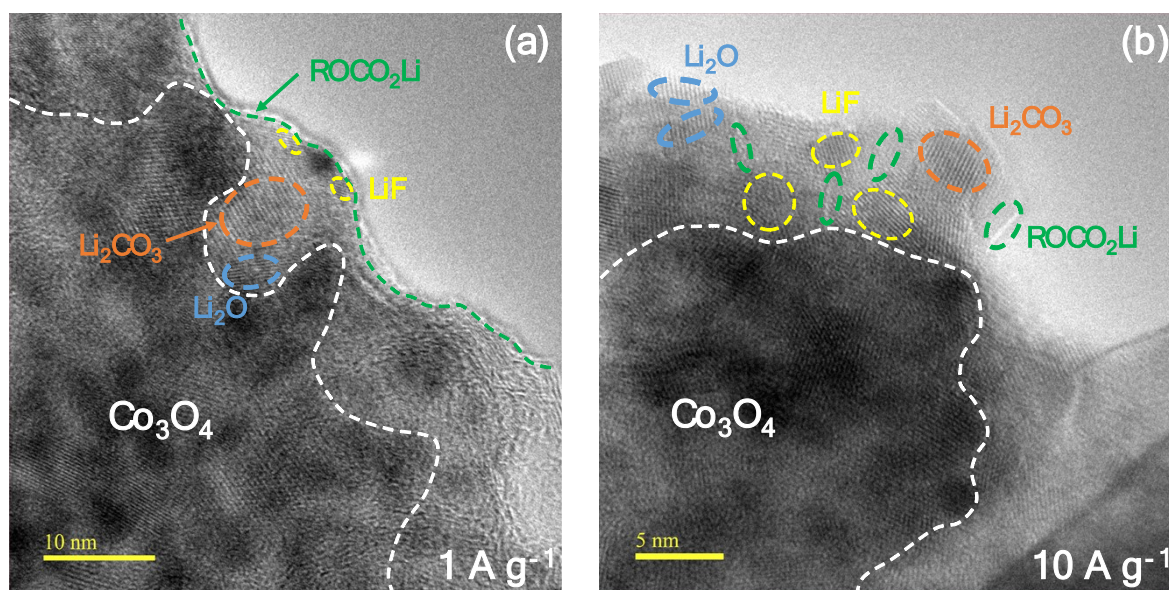

Figure S10. HRTEM images of SEI of fully oxidized S-Co_3O_4 after 10 cycles at (a) 1 A g^{-1} and (b) 10 A g^{-1}. The LiF (yellow dotted line) lattice spacing corresponding to (111) is ~0.23 nm, the Li_2CO_3 (orange dotted line) lattice spacing corresponding to (-

110) is ~0.42 nm, (-112) is ~0.26 nm, and the Li_2O (blue dotted line) lattice spacing corresponding to (111) is ~0.27 nm. The green dotted line represents the organic component $ROCO_2Li$ (OC = O) in the SEI.

The mosaic SEI was composed of randomly distributed organic and inorganic components at 10 A g^{-1}, which the organic component ($ROCO_2Li$) was an outer layer and the inorganic component was wrapped in an inner layer at 1 A g^{-1}. The layered configuration at 1 A g^{-1} led to the poor flexibility of the SEI and the unsatisfactory stability of the LIB for long cycle. On the contrary, the random distribution of $ROCO_2Li$ in the mosaic SEI at 10 A g^{-1} could enhance the flexibility of the SEI, accelerate the Li$^+$ transport and maintain good stability of the LIB.[2]
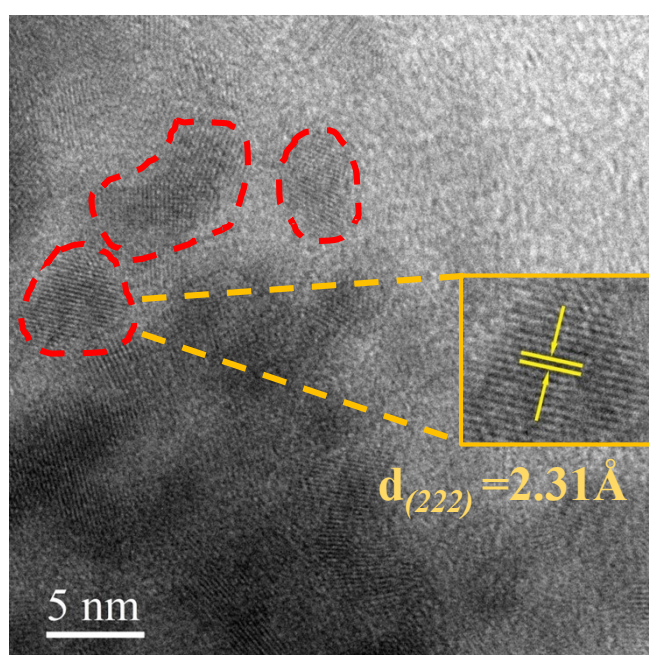

Figure S11. HRTEM image of the S-Co_3O_4 electrode after 2000 cycles at 10 A g^{-1}.
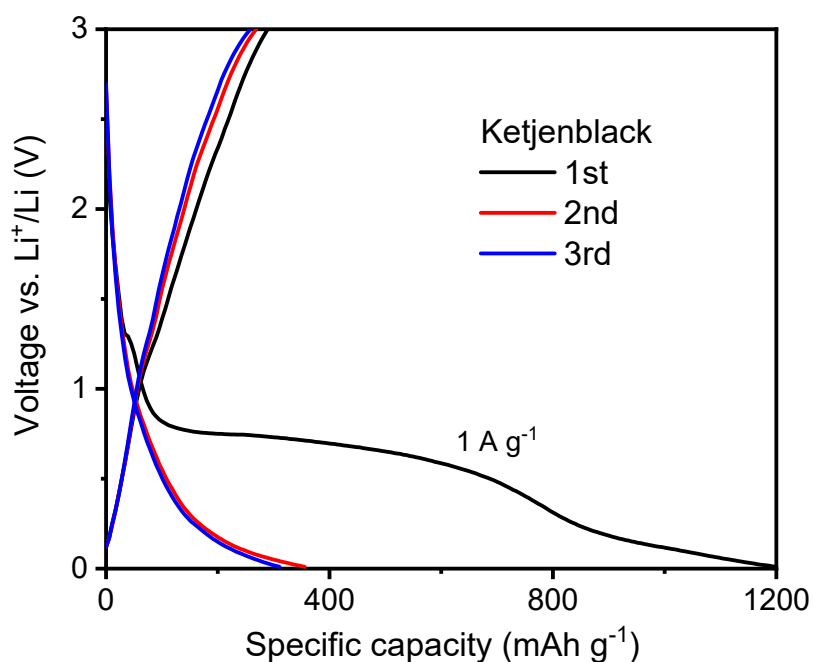
Figure S12. The initial three charge/discharge curves at a current density of 1 A g^{-1}

for Ketjenblack.

Ketjenblack and PVDF were mixed fully with a weight ratio of 9:1. Then made and

tested in the same way as Co_3O_4. The first discharge and charge specific capacities of

Ketjenblack are 1200.0 mAh g^{-1} and 289.6 mAh g^{-1}.

Table S1. Performances of recently reported LIBs (half-cell) based on Co_3O_4.

Co_3O_4	Voltage, V (*vs.* Li$^+$/Li)	Capacity, mAh g^{-1}	Cycling stability, [a] mAh g^{-1}	Refs.
RGO-Co_3O_4 PNR Co_3O_4 PNR	0.01-3	1118 @ 0.2 A g^{-1} 1049 @ 0.2 A g^{-1}	1118 @ 200th @ 0.5 A g^{-1} 526 @ 200th @ 0.5 A g^{-1}	3
Co3O4@NGFs	0.01-3	766.4 @ 0.1 A g^{-1}	408.4 @ 600th @ 2 A g^{-1}	4
H-Co3O4@IEH-Graphene	0.01-3	777 @ 0.2 A g^{-1}	1015 @ 250th @ 0.2 A g^{-1}	5

Co3O4 nanotubes	0.01-3	500 @ 0.05 A g^{-1}	500 @ 100th @ 0.48 A g^{-1}	6
Co3O4/graphene	0.01-3	800 @ 0.05 A g^{-1}	935 @ 30th @ 0.05 A g^{-1}	7
Needle-like Co3O4 nanotubes	0.01-3	918 @ 0.05 A g^{-1}	380 @ 80th @ 0.05 A g^{-1}	8
Co3O4NW arrays	0.01-3	700 @ 0.11 A g^{-1}	450 @ 20th @ 20 C 240 @ 20th @ 50 C	9
C-doped Co3O4 HNTs	0.01-3	950 @ 0.5 A g^{-1}	950 @ 300th @ 0.5 A g^{-1}	10
ZnO-Co3O4@CC	0.01-3	1785 @ 0.2 A g^{-1}	533.6 @ 400th @ 1 A g^{-1} 447.8 @ 400th @ 2 A g^{-1}	11
HNc-Co3O4	0.01-3	1053 @ 0.1 mA cm^{-1}	~600 @ 100th @ 0.1 mA cm^{-1}	2
Co3O4(1000)	0.01-3	~650 @ 1 A g^{-1}	1100 @ 150th @ 1 A g^{-1}	12
Co3O4	0.01-3	~1200 @ 1 A g^{-1}	927 @ 850th @ 1 A g^{-1}	13
S-Co3O4	0.01-3	**1686.7 @ 0.1 A g-1**	**511.2 @ 2000th @ 10 A g-1**	**This work**

[a] (Cycling stability is expressed as the energy storage capacity retention after several charging/discharging cycles at a specific rate).

Table S2. Performances of recently reported LIBs (half-cell) based on different types of anode materials.

Types	Materials	Voltage, V (vs. Li$^+$/Li)	Capacity, mAh g^{-1}	Cycling stability, [b] (capacity, rate, retention%)	Refs.
Oxides	Fe$_3$O$_4$-α-Fe$_2$O$_3$	0.005-3	1100 (0.1 A g^{-1})	40 (1067, 0.1 A g^{-1}, 97%)	14
	γ-Fe$_2$O$_3$ extracted from red mud	0.005-3	697 (0.15 A g^{-1})	60 (5433, 0.15 A g^{-1}, 78%)	15
	Fe$_3$O$_4$–HPGN	0.005-3	1002 (0.1 A g^{-1})	25 (900, 0.1 A g^{-1}, ~90%)	16

Category	Material	Voltage range (V)	Capacity (mAh g⁻¹)	Cycling stability	Ref.
	SnO_2-TRG	0.005-2.5	1021 (0.1 A g⁻¹)	100 (777, 0.5 A g⁻¹, 66%)	17
	SCM-TiO_2	1-3	220 (0.15 A g⁻¹)	250 (150, 0.15 A g⁻¹, 68%)	18
	$CuCo_2O_4$ nano wall	0.01-3	836 (1.25C)	120 (550, 0.375C, 61%)	19
	MOF-derived CuO	0.01-3	535 (0.1 A g⁻¹)	40 (481, 0.1 A g⁻¹, 90%)	20
Sulfides	Cu_3SnS_4	0.01-3	1082 (0.2 A g⁻¹)	950 (890, 0.5 A g⁻¹, 76%,)	21
	SnS_2-RGO-SnS_2 layer by layer	0.01-3	1404 (0.1 A g⁻¹)	200 (1357, 0.1 A g⁻¹, 97%) (909, 0.5 A g⁻¹, 90%)	22
Carbides	Fe_3SnC@CNF	0.01-3	573 (0.2 A g⁻¹)	1000 (500, 0.2 and 1 A g⁻¹, 96%)	23
	VC@C	0.01-3	640 (0.1 A g⁻¹)	1000 (440, 0.1 and 1 A g⁻¹, 82%)	24
	MXene	0.01-3	350 (0.1 A g⁻¹)	1000 (330, 0.1 A g⁻¹, 94%)	25
	PMo_{12}@PPy/$Ti_3C_2T_x$	0.01-3	395 (0.1 A g⁻¹)	300 (764, 0.1 A g⁻¹, 254%) 2000 (170, 3 A g⁻¹, ~340%)	26
Metal–organic framework (MOF)	Cu-BDC	0.01-2.5	194 (0.48 A g⁻¹)	50 (161, 0.48 A g⁻¹, 83%)	27
	Mn-BTC	0.01-2	694 (0.103 A g⁻¹)	100 (576, 0.103 A g⁻¹, 83%) (~400, 1 A g⁻¹, ~90%)	28
	Co-MOF (BDC)	0.01-3	1564 (0.1 A g⁻¹)	700 (601, 0.1 and 0.5 A g⁻¹, ~67%) 1000 (435, 0.1 and 1 A g⁻¹, 76%)	29
	dual ligand Fe-MOF (DMA cation)	0.01-3	600 (0.25 A g⁻¹)	100 (825, 0.25 A g⁻¹, 137%) 1100 (~460, 1 and 2 A g⁻¹, 99%)	30
Covalent-organic framework (COF)	Tp-Azo COF	0.01-3	623 (0.1 A g⁻¹)	3000 (306, 1 A g⁻¹, 100%)	31
	IISERP-CON	0.01-3	720 (0.1 A g⁻¹)	1000 (~580, 0.5 A g⁻¹, 98%)	32

	$CH_3NH_3PbBr_3$	0.01-2	332 (0.2 A g^{-1})	200 (121, 0.2 A g^{-1}, 36%)	33
	1D-benzidine lead iodide	0.01-2.5	646 (0.1 A g^{-1})	50 (585, 0.1 A g^{-1}, 91%)	34
Hybrid perovskite	iodo bismuthate				35
	I. ADB (1D)	0.01-2.5	520 (0.1 A g^{-1})	250 (~530, 0.1 A g^{-1}, ~62%)	
	II. IMB (0D)	0.01-2.5	450 (0.1 A g^{-1})	250 (~400, 0.1 A g^{-1}, ~77%)	
	III. ATB (1D)	0.01-2.5	230 (0.1 A g^{-1})	250 (~220, 0.1 A g^{-1}, ~44%)	
This work	**S-Co$_3$O$_4$**	**0.01-3**	**1686.7 @ 0.1 A g^{-1}**	**2000 (511.2, 10 A g^{-1}, 45%)**	

[b] Cycling stability is expressed as the energy storage capacity retention and corresponding retention percentage after several charging/discharging cycles at a specific rate.

E. g:

"200 (121, 0.2 A g^{-1}, 36%)" means that the cell can cycle to 200th at 0.2 A g^{-1}, with a 36% capacity retention of 121 mAh g^{-1}.

"1000 (435, 0.1 and 1 A g^{-1}, 76%)" means that the cell can cycle to 1000th at 1 A g^{-1} after activation at 0.1 A g^{-1} for several cycles, with a 76% capacity retention of 435 mAh g^{-1}.

Supplementary Reference

1.   M. A. Islam, M. Zuba, V. DeBiase, N. Noviasky and C. J. Hawley, *Nanotechnology*, 2018, **29**, 075403.

2. Y. Xiang, Y. Xu, Z. Yang, J. Na, A. Alowasheeir, M. D. Albaqami, A. Ahmed Awadh Bahajjaj, S. Wang, J. Yu and Y. Yamauchi, *Chem. Eng. J.*, 2022, **430,** 132700.

3. J. Shi, X. Li, T. Yang, X. Tian, Y. Liu, S. Lei, Y. Song and Z. Liu, *Journal of Materials Science*, 2021, **56**, 7520-7532.

4. Y. Chen, T. Wu, W. Chen, W. Zhang, L. Zhang, Z. Zhu, M. Shao, B. Zheng, S. Li, W. Zhang, W. B. Pei, J. Wu and F. Huo, *Chem Commun (Camb)*, 2020, **56**, 5767-5770.

5. D. Wu, C. Wang, H. Wu, S. Wang, F. Wang, Z. Chen, T. Zhao, Z. Zhang, L. Y. Zhang and C. M. Li, *Carbon*, 2020, **163**, 137-144.

6. W. Y. Li, L. N. Xu and J. Chen, *Adv. Funct. Mater.*, 2005, **15**, 851-857.

7. W. C. R. Z. S. Wu, L. Wen, L. B. Gao, J. P. Zhao, Z. P. Chen, G. M. Zhou, F. Li, H. M. Cheng, *ACS nano*, 2010, **4**, 3187.

8. X. W. Lou, D. Deng, J. Y. Lee, J. Feng and L. A. Archer, *Adv. Mater.*, 2008, **20**, 258-262.

9. B. T. a. Y. G. Li, Y. Y. Wu, *Nano Lett.*, 2008, **8**, 265.

10. C. Yan, Y. Zhu, Y. Li, Z. Fang, L. Peng, X. Zhou, G. Chen and G. Yu, *Adv. Funct. Mater.*, 2018, **28,** 1705951.

11. H. Chen, L. Deng, S. Luo, X. Ren, Y. Li, L. Sun, P. Zhang, G. Chen and Y. Gao, *J. Electrochem. Soc.*, 2018, **165**, A3932-A3942.

12. J. Y. Cheong, J. H. Chang, S.-H. Cho, J.-W. Jung, C. Kim, K. S. Dae, J. M. Yuk and I.-D. Kim, *Electrochim. Acta*, 2019, **295**, 7-13.

13. H. Sun, G. Xin, T. Hu, M. Yu, D. Shao, X. Sun and J. Lian, *Nat Commun*, 2014, **5**, 4526.

14. M. Biswal, A. Suryawanshi, V. Thakare, S. Jouen, B. Hannoyer, V. Aravindan, S. Madhavi and S. Ogale, *J. Mater. Chem. A*, 2013, **1,** 13932-13940.

15. A. Suryawanshi, V. Aravindan, S. Madhavi and S. Ogale, *ChemSusChem*, 2016, **9**, 2193-2200.

16. A. Suryawanshi, V. Aravindan, D. Mhamane, P. Yadav, S. Patil, S. Madhavi and S. Ogale, *Energy Storage Materials*, 2015, **1**, 152-157.

17. D. Mhamane, V. Aravindan, D. Taneja, A. Suryawanshi, O. Game, M. Srinivasan and S. Ogale, *Compos. Sci. Technol.*, 2016, **130**, 88-95.

18. O. Game, T. Kumari, U. Singh, V. Aravindan, S. Madhavi and S. B. Ogale, *Energy Storage Materials*, 2016, **3**, 106-112.

19. M. Bhardwaj, A. Suryawanshi, R. Fernandes, S. Tonda, A. Banerjee, D. Kothari and S. Ogale, *Mater. Res. Bull.*, 2017, **90**, 303-310.

20. A. Banerjee, U. Singh, V. Aravindan, M. Srinivasan and S. Ogale, *Nano Energy*, 2013, **2**, 1158-1163.

21. N. Sharma, D. Phase, M. O. Thotiyl and S. Ogale, *ChemElectroChem*, 2019, **6**, 1371-1375.

22. Y. Jiang, D. Song, J. Wu, Z. Wang, S. Huang, Y. Xu, Z. Chen, B. Zhao and J. Zhang, *ACS Nano*, 2019, **13**, 9100-9111.

23. K. Roy, V. Chavan, S. M. Hossain, S. Haldar, R. Vaidhyanathan, P. Ghosh and S. B. Ogale, *ChemSusChem*, 2020, **13**, 196-204.

24. M. Mahajan, K. Roy, S. Parmar, G. Singla, O. P. Pandey, K. Singh, R. Vaidhyanathan and S. Ogale, *Carbon*, 2020, **161**, 108-116.

25. A. Sengupta, B. V. B. Rao, N. Sharma, S. Parmar, V. Chavan, S. K. Singh, S. Kale and S. Ogale, *Nanoscale*, 2020, **12**, 8466-8476.

26. M. Mahajan, G. Singla and S. Ogale, *ACS Applied Energy Materials*, 2021, **4**, 4541-4550.

27. R. Senthil Kumar, C. Nithya, S. Gopukumar and M. Anbu Kulandainathan, *Energy Technology*, 2014, **2**, 921-927.

28. S. Maiti, A. Pramanik, U. Manju and S. Mahanty, *ACS Appl Mater Interfaces*, 2015, **7**, 16357-16363.

29. C. Li, X. Hu, X. Lou, L. Zhang, Y. Wang, J.-P. Amoureux, M. Shen, Q. Chen and B. Hu, *J. Mater. Chem. A*, 2016, **4**, 16245-16251.

30. N. Sharma, S. Szunerits, R. Boukherroub, R. Ye, S. Melinte, M. O. Thotiyl and S. Ogale, *ACS Applied Energy Materials*, 2019, **2**, 4450-4457.

31. G. Zhao, Y. Zhang, Z. Gao, H. Li, S. Liu, S. Cai, X. Yang, H. Guo and X. Sun, *ACS Energy Letters*, 2020, **5**, 1022-1031.

32. S. Haldar, K. Roy, S. Nandi, D. Chakraborty, D. Puthusseri, Y. Gawli, S. Ogale and R. Vaidhyanathan, *Adv. Energy Mater.*, 2018, **8,** 1702170.

33. H. R. Xia, W. T. Sun and L. M. Peng, *Chem Commun (Camb)*, 2015, **51**, 13787-13790.

34. M. Tathavadekar, S. Krishnamurthy, A. Banerjee, S. Nagane, Y. Gawli, A. Suryawanshi, S. Bhat, D. Puthusseri, A. D. Mohite and S. Ogale, *J. Mater. Chem. A*, 2017, **5**, 18634-18642.

35. K. Roy, T. Li, S. Ogale and N. Robertson, *J. Mater. Chem. A*, 2021, **9**, 2689-2693.